ACS SENSORS

pubs.acs.org/acssensors

Article

Gold Nano/Micro-Islands Overcome the Molecularly Imprinted Polymer Limitations to Achieve Ultrasensitive Protein Detection

Alireza Sanati, Roozbeh Siavash Moakhar, Imman I. Hosseini, Keyvan Raeissi, Fathallah Karimzadeh, Mahsa Jalali, Mahshid Kharaziha, Sara Sheibani, Laleh Shariati, John F. Presley, Hojatollah Vali, and Sara Mahshid*

Cite This: *ACS Sens.* 2021, 6, 797−807

Read Online

ACCESS | Metrics & More | Article Recommendations | Supporting Information

ABSTRACT: Here, we report on an electrochemical biosensor based on core−shell structure of gold nano/micro-islands (NMIs) and electropolymerized imprinted *ortho*-phenylenediamine (o-PD) for detection of heart-fatty acid binding protein (H-FABP). The shape and distribution of NMIs (the core) were tuned by controlled electrodeposition of gold on a thin layer of electrochemically reduced graphene oxide (ERGO). NMIs feature a large active surface area to achieve a low detection limit (2.29 fg mL^{-1}, a sensitivity of 1.34 × 10^{13} μA mM^{-1}) and a wide linear range of detection (1 fg mL^{-1} to 100 ng mL^{-1}) in PBS. Facile template H-FABP removal from the layer (the shell) in less than 1 min, high specificity against interference from myoglobin and troponin T, great stability at ambient temperature, and rapidity in detection of H-FABP (approximately 30 s) are other advantages of this biomimetic biosensor. The electrochemical measurements in human serum, human plasma, and bovine serum showed acceptable recovery (between 91.1 ± 1.7 and 112.9 ± 2.1%) in comparison with the ELISA method. Moreover, the performance of the biosensor in clinical serum showed lower detection time and limit of detection against lateral flow assay (LFA) rapid test kits, as a reference method. Ultimately, the proposed biosensor based on the core−shell structure of gold NMIs and MIP opens interesting avenues in the detection of proteins with low cost, high sensitivity and significantstability for clinical applications.

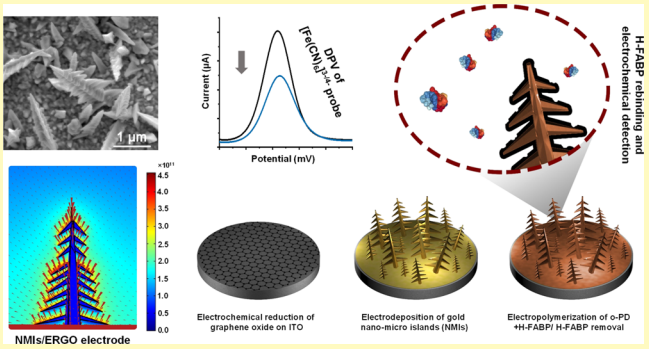

KEYWORDS: *cardiac biomarkers, electrochemical biosensors, heart-fatty acid binding protein (H-FABP), gold nano/micro-islands, molecularly imprinted polymers (MIPs)*

Molecularly imprinted polymers (MIPs), a group of biomimetic receptors, have gained significant attention as an alternative to antibody-based immunosensors owing to high stability at room temperature and a cost-effective fabrication process.[1−9] However, current challenges and limitations on the application of MIPs in biosensing are mainly focused on improving their selectivity, sensitivity, and ease of fabrication. In terms of selectivity, the combination of aptamers and MIPs is a promising approach.[10−12] Surface imprinting techniques and nanomaterial-conjugated MIPs can be successfully used to improve the sensitivity and simplify the fabrication process.[13,14] Specifically for proteins, template removal is the most challenging step in fabrication because it is usually performed at high temperatures and for several minutes using alkaline or acidic solutions.[2,15,16] Surface imprinting technology is one of the most promising methods for the fabrication of MIPs, via two common strategies.[17,18] First, by combining the template and monomer and subsequent polymerization, and second, by immobilizing protein on the surface and carrying out UV polymerization or electropolymerization.[19−22] The former can undesirably cause confinement of the protein in the polymeric layer, while in the latter, controlling thickness of the polymeric layer is crucial.[18,23] Thus, the fabrication of ultrathin and controllable polymeric layers with high sensitivity is known as another current challenge in the field of MIPs. Among various surface imprinting methods, electropolymerization provides a compact and ultrathin polymeric layer on the surface of the biosensor to enhance the read-out signal and sensitivity for detection of proteins,[24,25] peptides,[8] small molecules,[26] bacteria,[27] and metallic ions.[28] *Ortho*-phenylenediamine (o-PD) presents a

Received: August 15, 2020
Accepted: January 4, 2021
Published: January 19, 2021

https://dx.doi.org/10.1021/acssensors.0c01701
ACS Sens. 2021, 6, 797−807

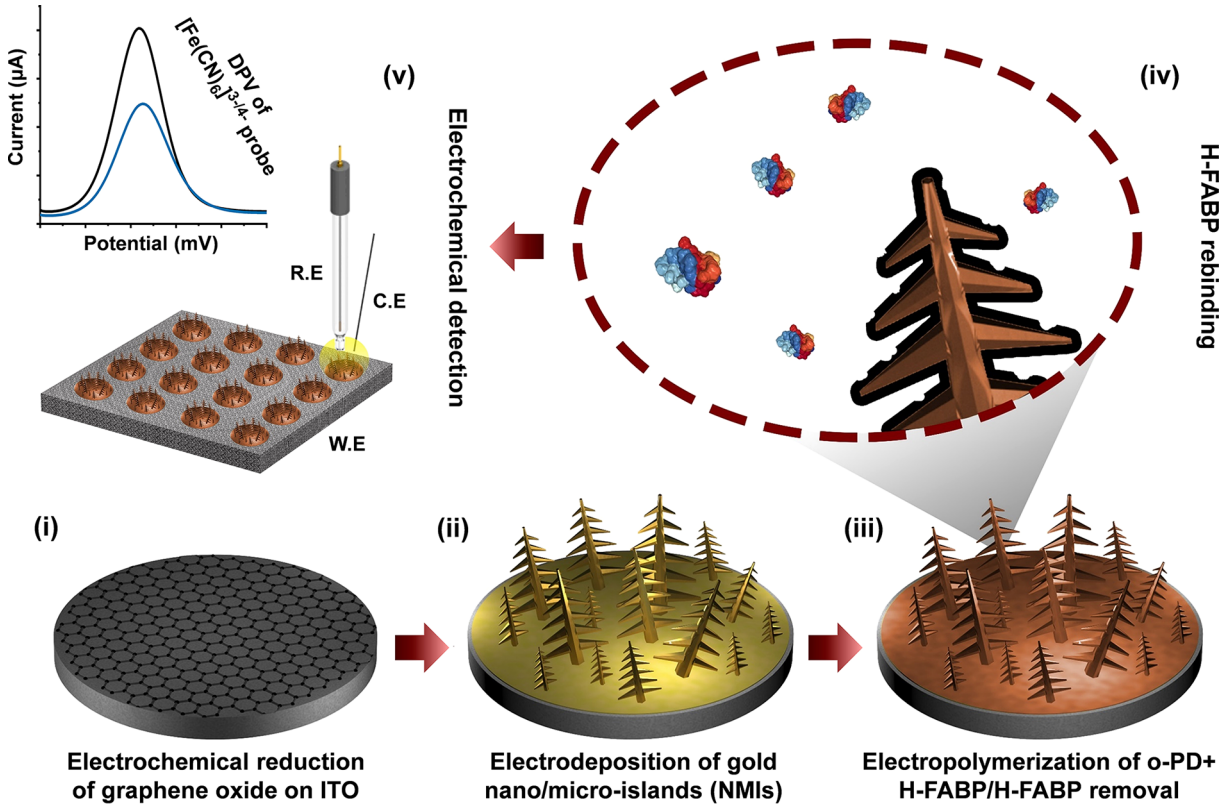

Figure 1. Stepwise schematic of the MIP biosensor fabrication and electrochemical detection of H-FABP. (i) Electrochemical reduction of graphene oxide on ITO, (ii) electrodeposition of NMIs, (iii) MIP biosensor fabrication through electropolymerization and template H-FABP removal, (iv) H-FABP rebinding, and (v) subsequent electrochemical detection of H-FABP using the $[Fe(CN)_6]^{3-/4-}$ probe. Black and blue diagrams are related to before and after H-FABP rebinding, respectively. C.E: counter electrode, R.E: reference electrode, and W.E: patterned working electrodes. The diameter of each individual electrode is 1 mm.

good biocompatibility behavior against proteins and can be easily electropolymerized on gold electrodes.[29−31]

Nanomaterials are used in combination with MIPs (i) to increase the sensitivity and linear range of detection by offering a large active surface area, (ii) to facilitate the template removal during MIP fabrication[32,33] by increasing the number of surface atoms with higher energy than bulk atoms, and (iii) to generate a core−shell or composite structure with MIPs to simultaneously have the properties of the nanomaterial and MIP.[33−35]

We previously reported hierarchical gold nano/micro-islands (NMIs), with enhanced active surface area for optical and electrochemical sensing, whereas the NMIs were successfully implemented for detection of bacteria, antibodies, dopamine, and glucose.[36−42] In this work, we report on a hybrid structure of NMIs and MIP to develop an electrochemical biosensor for detection of heart fatty acid binding protein (H-FABP), a newly discovered cardiac biomarker, which is released in blood after 30−90 min of myocardial infarction (MI). Compared to myoglobin and troponin—two well-known cardiac biomarkers—H-FABP is 20 times more specific than myoglobin and shows higher sensitivity than troponin in the first hours of MI.[43]

There are few studies on electrochemical detection of H-FABP, in which antibody-based capturing probes are immobilized on carbon and gold nanostructured electrodes,[44−46] but to the best of our knowledge, there is no report on application of MIP/NMI electrodes. A stepwise schematic of the MIP biosensor fabrication and detection of H-FABP is presented in Figure 1. Briefly, at the heart of our biosensor, NMIs are electrodeposited on an indium−tin−oxide (ITO) substrate coated with a thin layer of electrochemically reduced graphene oxide (ERGO). The ERGO layer remarkably increased the active surface area of the electrode[47,48] and, subsequently, the nucleation sites for electrodeposition, to provide a more uniform distribution of gold on the surface.[49] Eventually, the MIP layer was electropolymerized on NMI-modified electrodes and exploited toward detection of H-FABP. NMIs feature a high surface area for deposition of MIP and can be effective on template H-FABP removal during MIP construction. We expect that this combination can successfully result in the fabrication of a simple, cost-effective, and sensitive biosensor for protein detection.

EXPERIMENTAL SECTION

Materials, apparatus, and electrode preparation are presented in the Supporting Information (see Section S1).

Preparation of the MIP Biosensor. Electrosynthesis of o-PD for cardiac biomarkers was carried out following a facile method as described elsewhere.[21,22] Briefly, a solution containing different concentrations of o-PD in 0.5 M acetate buffer was prepared using sodium acetate and acetic acid (pH was adjusted by HCl and NaOH to 5.2). H-FABP was added to the solution with a concentration of 100 μg mL^{-1}, and the volume of the monomer solution to the protein solution was maintained in the ratio of 95:5. Furthermore, electropolymerization of o-PD on the NMIs/ERGO electrode was carried out using the cyclic voltammetry technique at a scan rate of 50 mV s^{-1} in the range of 0 to 0.8 V versus Ag/AgCl. Eventually, the samples were washed with ethanol and water solution (5:1 V/V)

https://dx.doi.org/10.1021/acssensors.0c01701
ACS Sens. 2021, 6, 797−807

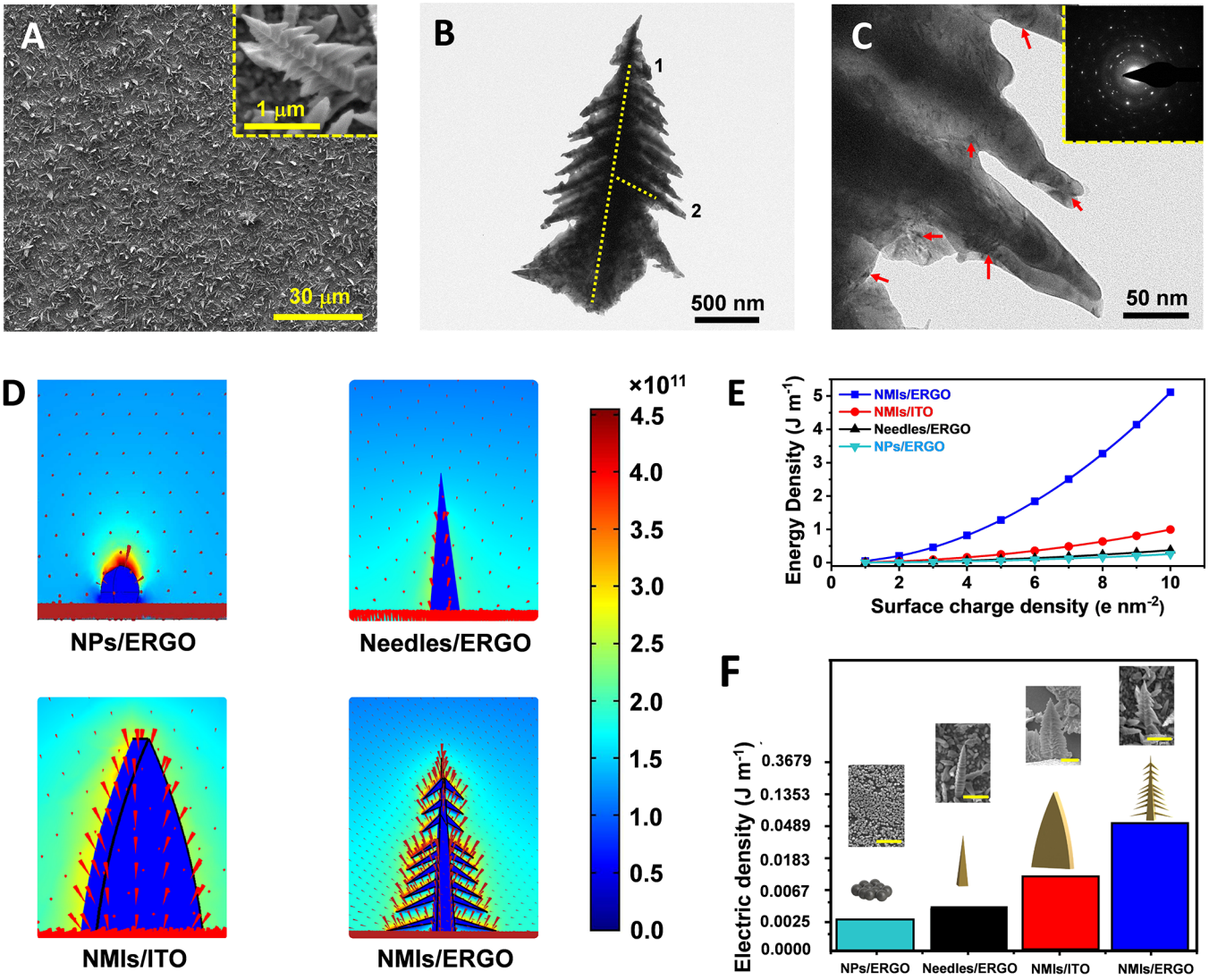

Figure 2. Microstructural properties and finite element simulation of the electric field on different electrodes. SEM images of the (A) NMIs/ERGO electrode (inset: high-magnification SEM image of NMIs), (B,C) TEM images of a gold shrub-like structure (arrows display imperfections, and the inset shows the corresponding SAED pattern). (D) 2D-contour of the electric field over four different electrodes: NPs/ERGO, needles/ERGO, NMIs/ITO, and NMIs/ERGO for 1 (e/k_BT). (E) Surface integration of energy density over the surface of the electrodes for different surface charge densities. (F) Comparison of surface integration of electric density (the symbolic images of each electrode with SEM images of each structure are included, scale bar: 1 μm).

containing 0.1 M NaOH to remove the template H-FABP. Similarly, a control NMIs/ERGO electrode modified by non-imprinted polymer (NIP) was fabricated without using H-FABP as the template protein.

Sensing Performance of the MIP Biosensor. A 10 mM phosphate-buffered saline (PBS) solution and diluted human serum (HS) were separately spiked with various concentrations of H-FABP, troponin T (TnT), and myoglobin (Myo), incubated on the surface of each electrode for 30 s, and followed by rinsing with deionized water (DIW) to remove unattached proteins and drying. A similar method was used for diluted human plasma (HP) and bovine serum (BS), as well as clinical samples. Differential pulse voltammetry (DPV) was applied at ambient temperature using a 10 mM PBS solution containing 5 mM $[Fe(CN)_6]^{3-/4-}$ (1:1 V/V) for monitoring MIP fabrication and sensing performance. DPV measurements were performed in the range of 0 to 0.5 V versus Ag/AgCl. A step potential of 4 mV, a modulation time of 0.05 s, a modulation amplitude of 0.05 V, and a scan rate of 50 mV s^{-1} were used for this aim.

Clinical Sample Collection. To investigate the performance of the developed H-FABP MIP biosensor under clinical conditions, the human blood serum samples were collected from patients with symptoms of chest pain, ST-segment and troponin I (TnI: another important cardiac biomarker) elevation, typical of MI. The patients were admitted at the intensive care unit (ICU) and coronary care unit (CCU) sections of "Noor and Hazrat-e-Ali Asghar" hospital, an Isfahan University of Medical Sciences-affiliated hospital in Isfahan, Iran. Human serum collected from adult healthy patients with no underlying MI symptoms was used as the negative control in this study. The ethics approval for the study protocol was reviewed and confirmed by the institutional review boards (IRB) at McGill University and Isfahan University of Medical Sciences (Approval IDs: A11-M66-20A (20-11-056) and IR.MUI.MED.REC.1399.820). Before electrochemical investigations, clinical serums were diluted with 10 mM PBS.

LFA Studies. Lateral flow assay (LFA) cassettes, as an immunoassay antibody-based colorimetric rapid test, were received from Home Health UK company and used as a qualitative reference method to explore the performance of the developed MIP biosensor in clinical samples. The cassettes were a combo device to simultaneously examine H-FABP and TnI in blood/serum/plasma. The limit of detection for this device reported by the company was 8

https://dx.doi.org/10.1021/acssensors.0c01701
ACS Sens. 2021, 6, 797−807

ng mL^{-1} for H-FABP and 0.5 ng mL^{-1} for TnI. Therefore, before investigating the performance of the MIP biosensor against clinical samples, they were tagged as negative and positive H-FABP and TnI by the LFA cassettes. According to the company's instructions, after dropping 50 μL of clinical serum samples and 40 μL of the buffer solution (provided by the company) on the specimen area and waiting for 10 min, the appeared colored line(s) was(were) investigated.

Finite Element Simulation. Finite element simulation is performed to evaluate the effect of NMIs/ERGO on the electrical field in COMSOL Multiphysics (version 5.5, COMSOL, Inc.). The geometry was made in SolidWorks (version 2020, Dassault Systems) based on statistical scanning electron microscopy (SEM) images. The analysis was performed over four different structures including gold nanoparticles (NPs)/ERGO (deposited using 5 mM $HAuCl_4$ at −0.4 V vs Ag/AgCl for 50 s), gold needles/ERGO (deposited using 50 mM $HAuCl_4$ at 0.0 V vs Ag/AgCl for 50 s), NMIs/ITO (deposited using 100 mM $HAuCl_4$ at 0.0 V vs Ag/AgCl for 50 s), and NMIs/ERGO (deposited using 100 mM $HAuCl_4$ at 0.0 V vs Ag/AgCl for 50 s). The diameter of NPs was 0.1 μm, and the gold needle was considered a square with 0.3 μm on each side. The height of the needle was 1.5 μm. The NMIs/ITO was considered to have 1.7 μm width and a very small thickness of 0.3 μm with a height of 2.8 μm. Finally, the NMIs/ERGO was made similar to needles/EGRO and the shrubs were added with a final height of 2.2 μm, 1.2 μm width, and a thickness of 0.4 μm. The electrostatic module was used to simulate the electrical field. In this simulation, the surface of the structures was homogenously charged. The structures are placed in a half-sphere environment, and the infinite element domain is used to apply zero potential in infinity.

RESULTS AND DISCUSSION

Choice of Materials. Material selection in defining a biosensor is always the most important of the initial stages. In biosensing, a combination of high electrical conductivity, surface area, and stability, as well as facile fabrication processes, is suggested to reach a high sensitivity, wide linear range of detection, and high stability. ITO as a cost-effective and conductive glass can be used for electrodeposition of a wide range of materials. For increasing the surface area of ITO, we modified the surface with ERGO. Gold electrodes with high electrical conductivity and chemical stability are widely used for electrochemical biosensing. To reach a high surface area and high sensitivity with a facile methodology, we used electrodeposited 3D gold NMIs on the surface. The NMIs with spatial orientation and tunable nanorough protrusions provide enhanced sensitivity and quantifiable detection in electrochemical and optical sensors.[36,39,41] The proposed electrode possesses higher chemical stability than silver nanoparticle-based devices[50] along with an easier fabrication process than ZnO, MoS_2, carbon quantum dots, and other oxides or sulfides used in biosensing.[41,51−54] Ultimately, in order to reach high stability, we used o-PD as a typical nonconductive monomer for electropolymerization and MIP/protein fabrication.[55,56] The o-PD monomer rather than conductive ones such as aniline and pyrrole can create ultrathin and stable polymeric layers comparable to the size of proteins and, consequently, provide high sensitivity and efficient surface imprinting.

Preparation and Characterization of the MIP Biosensor. We used different surface characterization techniques including SEM, transmission electron microscopy (TEM), and atomic force microscopy (AFM) to study the morphology, crystallinity, and structural properties of the fabricated electrodes. Figure 2A shows a uniform distribution of gold NMIs on the ERGO surface which is vital for sensor reproducibility and favorable sensing performance. From Figure 2B, the length of a single gold shrub is found to be about 2.2 μm (line 1). The microdimension of the gold electrode significantly improves electrical conductivity.[57] Figure 2C shows the enlarged TEM image of a single electrode containing nanoelectrodes with dimensions in the range of 50 to 300 nm (line 2 in Figure 2B). These nanoelectrodes provide high nanoroughness and active surface area for detection of protein (Figure S3). The arrows in Figure 2C indicate the presence of defects and dislocations in the structure, likely resulting from the induced local stress through the electrodeposition process.[58] The inset in Figure 2C displays the selected area electron diffraction (SAED) pattern of NMIs, signifying a combination of poly-nanocrystalline (dots) and amorphous (shade) areas. The dislocations and poly-nanocrystalline and amorphous areas act as catalytic active sites which enhance the entropy, surface energy, and electroactivity of the structure.[59−61] This will favor a high level of reaction with the washing solution, simplify the template removal during MIP construction, and increase the catalytic activity, with a final result of higher sensitivity. Increasing the catalytic activity that resulted from crystalline defects improves the electron transfer rate at the electrode/electrolyte interface. Consequently, lower amounts of analytes can be detected easily and with higher sensitivity. The performance of NMIs/ERGO (containing defective needle shape structures) and NPs/ERGO electrodes in template removal is presented in Figure S4C.

We exploited finite element simulation to analyze the effect of nanostructuring on the electric field and consequently the electrode sensibility. Different gold electrodes were successfully modeled in COMSOL Multiphysics. Based on the SEM images, four different electrodes are drawn including NPs/ERGO, needles/ERGO, NMIs/ITO, and NMIs/ERGO. The electric field distribution surrounding the structure is evaluated by considering a uniform charge density (1 e nm^{-2}) on the surface of the structure (Figure 2D). Accordingly, the appendage needles from the backbone provide a highly local electric field, which can boost charge transformation and oxidation rate in electrochemical investigations. Surface integration of energy density over the surface of the structure represents the charge transferability of the structure and consequently lower LOD.[59] Figure 2E shows the relation between energy density and surface charge density for four different structures. The energy density depends on the surface area and the electric field surrounding the structure and increases exponentially with surface charge density. Figure 2F shows the value of electric field density over the surface of different structures when the surface charge density is 1 (e nm^{-2}) and the comparison of the model used in simulation and SEM images. The defective structure of NMIs/ERGO electrodes and their high surface area (Section S4) result in high local electric fields and provide considerably higher energy density per surface area in comparison to the normal electrodes, which yield high sensitivity.[59] Thus, in the next sections, we have considered this electrode as a core for the MIP (shell) layer. Electropolymerization and optimization of the MIP layer are presented and discussed in the Supporting Information (see Section S5).

AFM and TEM were further used to evaluate the fabricated MIP structure. AFM observations can be employed to validate the successful removal of H-FABP from the polymeric matrix.[55,62] Figure 3A,B represents the AFM micrographs

https://dx.doi.org/10.1021/acssensors.0c01701
ACS Sens. 2021, 6, 797−807

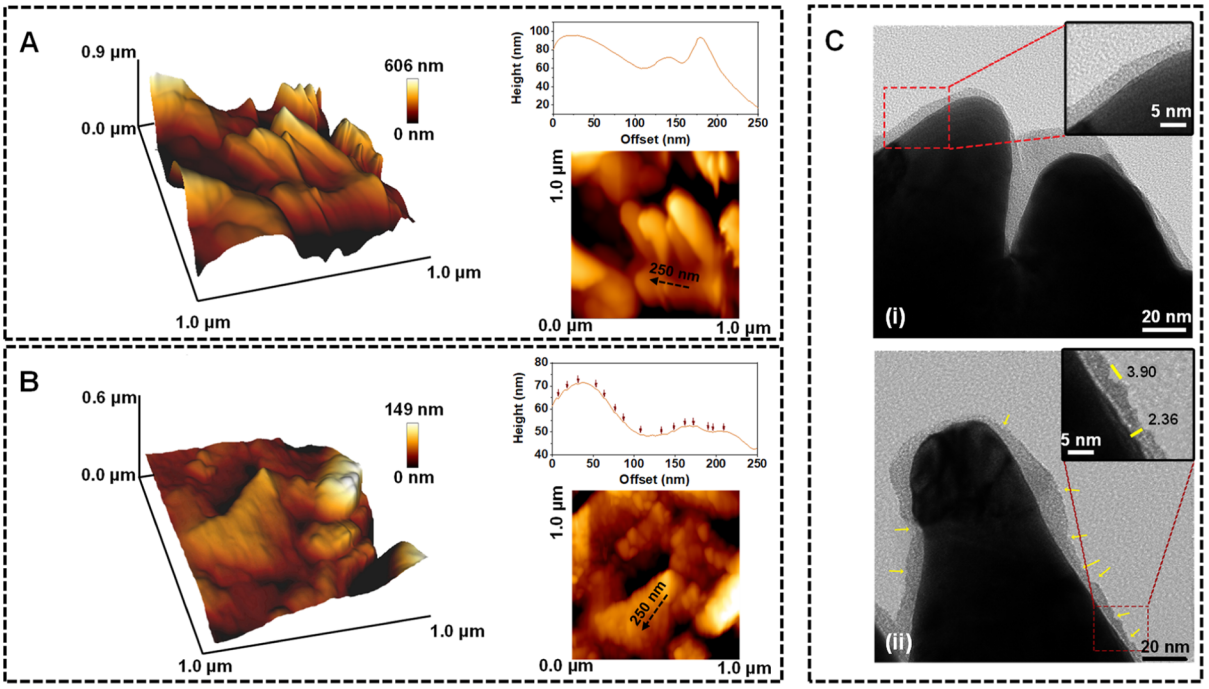

Figure 3. Microstructural characteristics of the MIP biosensor. The 3D and 2D AFM micrographs and cross-sectional AFM profiles of (A) NIP and (B) MIP electrodes. (C) TEM image of the MIP electrode: (i) before and (ii) after washing with the optimal solution (inset: the clarified imprinted sites with arrows).

and cross-sectional profiles of the NIP and MIP electrodes, respectively. The MIP surface seems to be rougher relative to NIP. The red arrows in the cross-sectional profiles highlight the valleys, signifying the successful H-FABP removal. This observation is in agreement with previous studies.[55,62]

Further characterization of the MIP structure was carried out by TEM investigations. Figure 3C(i) depicts the TEM images of the core−shell structure of the MIP electrode before template removal. The dark area and the ultrathin gray layer are corresponded to gold (core) and MIP (shell), respectively. The average thickness of this layer is approximately 5.5 ± 0.5 nm. The inset shows a very smooth and uniform layer of o-PD before H-FABP removal. This ultrathin layer is also beneficial to facilitate H-FABP removal during the MIP construction. After washing the electrode with the optimal solution, the imprinted sites are created [highlighted with yellow arrows in Figure 3C(ii)]. The inset clearly shows the imprinted sites in the o-PD matrix, where the sizes of an imprinted site are comparable with the calculated size of H-FABP (Section S5).

Analytical Performance of the MIP Biosensor. The optimized MIP biosensor was used to quantitate H-FABP in the range of 1 fg mL^{-1} to 100 ng mL^{-1}. Figure 4A demonstrates the DPV responses of the MIP biosensor with different H-FABP concentrations in a 10 mM PBS solution containing 5 mM $[Fe(CN)_6]^{3-/4-}$ (pH 7.4). The current (I_{pa} of $[Fe(CN)_6]^{3-/4-}$) linearly decreases with an increase in H-FABP concentration over the range of 1 fg mL^{-1} to 100 ng mL^{-1}, according to current (μA) = 10.3−0.89 log[H-FABP] (fg mL^{-1}). Also, the positive shift of the oxidation potential with increasing H-FABP concentration indicates the rebinding of H-FABP on the surface, decreasing the electron transfer rate and decreasing oxidation of $[Fe(CN)_6]^{4-}$ to $[Fe(CN)_6]^{3-}$. The LOD was calculated by dividing three times the standard deviation of the blank (Sb = 0.68) by the slope of the calibration plot (3Sb/0.89) equal to 2.29 fg mL^{-1} (Figure 4A). Also, the analytical sensitivity based on the slope of the calibration plot (μA mM^{-1})/active surface area (0.45 ± 0.05 cm^2)[63] was calculated to be 1.34 × 10^{13} μA mM^{-1}, which shows an ultrahigh sensitivity. The physiological concentration range of H-FABP in human serum for a healthy adult is reported as 3.9 ng mL^{-1}. When MI occurs, this value will increase to 15.6 ng mL^{-1}.[64] Also, it should be considered that under the clinical conditions, cardiac biomarker evaluations are usually performed in the range of pg mL^{-1} (or lower) to several hundreds of ng mL^{-1} in order to accurately monitor the MI patients.[40,65] Interestingly, the MIP/NMIs biosensor not only functions in the biological range of H-FABP but also detects very low values of proteins. Even though an ultrahigh sensitivity may not be a necessity for detection of H-FABP, our results suggest that the hybrid structure of MIP/NMIs could efficiently be applied for highly sensitive detection of a wide biological range of proteins. Moreover, the wide linear range of detection is mainly attributed to the high number of imprinted sites (4.80 × 10^{12}; calculated in Section S5) related to the large active surface area of NMIs.

Our biosensor possesses a low LOD and a wide linear range compared to other reported values in the literature (Table S1), which is attributed to the high active surface area and superb electrochemical performance of the NMIs. We also compared the performance of the NIP and MIP electrodes with H-FABP spiked at four distinct concentrations in a 10 mM PBS solution (Figure 4B). Here, we assessed the performance of the biosensor by defining $(I_0 - I)/I_0$ parameter, where I_0 is I_{pa} of $[Fe(CN)_6]^{3-/4-}$ recorded in DPV test in the absence of H-FABP and I is I_{pa} of $[Fe(CN)_6]^{3-/4-}$ in DPV test in the presence of H-FABP on the electrode. The changes in $(I_0 - I)/I_0$ with concentration are negligible for the NIP electrode with a lower slope [0.0063 (fg^{-1} mL) compared to the MIP (0.0715 fg^{-1} mL)], indicating that the NIP electrode is incapable of detecting H-FABP.

https://dx.doi.org/10.1021/acssensors.0c01701
ACS Sens. 2021, 6, 797−807

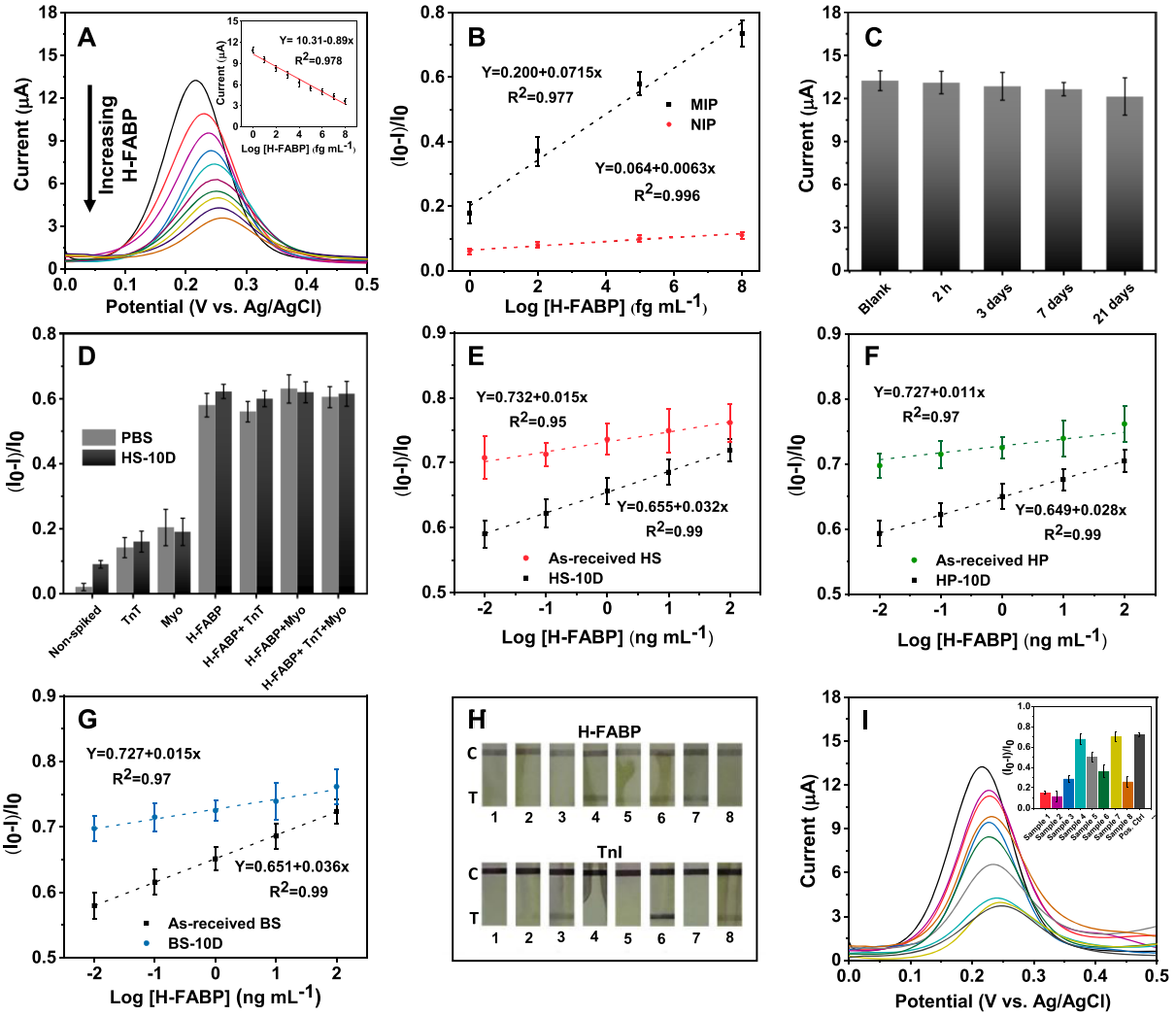

Figure 4. MIP biosensing properties. (A) DPVs and calibration plot (inside) of the MIP biosensor in 10 mM PBS spiked with various H-FABP concentrations (1 fg mL^{-1} to 100 ng mL^{-1}). (B) Comparison of the performance of the MIP and NIP electrodes in 10 mM PBS spiked with various H-FABP concentrations. (C) Stability of the developed MIP biosensor. (D) Bar charts for the selectivity performance of the MIP electrode in nonspiked 10 mM PBS, 10 times diluted human serum (HS-10D) and spiked PBS and HS-10D with 100 pg mL^{-1} H-FABP, 100 pg mL^{-1} myoglobin (Myo), 100 pg mL^{-1} troponin T (TnT), 100 pg mL^{-1} H-FABP + 1 ng mL^{-1} Myo, 100 pg mL^{-1} H-FABP + 1 ng mL^{-1} TnT, and 100 pg mL^{-1} H-FABP + 1 ng mL^{-1} TnT+ 1 ng mL^{-1} Myo. (E), (F), and (G) Comparison of the performance of the MIP biosensor versus the clinical range of H-FABP in the as-received and 10 times diluted (10D) human serum (HS), human plasma (HP), and bovine serum (BS), respectively. (H) Photographs of the LFA examinations of clinical samples (C: control line; T: test line), and (I) DPV plots and related bar charts of the MIP biosensors for detection of clinical samples. Positive control (Pos. Ctrl) is HS-10D spiked with 100 ng mL^{-1} H-FABP. The electrochemical results are obtained in a 10 mM PBS solution containing 5 mM $[Fe(CN)_6]^{3-/4-}$ before and after incubation of protein solutions on the electrode (n = 3).

Stability, Repeatability, and Reproducibility of the MIP Biosensor. One of the major advantages of MIP biosensors over antibody-based biosensors is their high stability at ambient temperature.[7] Here, we examined the stability of the MIP biosensor during 21 days of storage at ambient temperature. The I_{pa} of $[Fe(CN)_6]^{3-/4-}$ for the MIP biosensor was recorded after 2 h, 3 days, 7 days, and 21 days of storage in a shelf. Figure 4C demonstrates that the current responses decrease by 4.4% and 8.4% after 7 and 21 days, respectively. These results indicate that the developed biosensor possesses high stability at the ambient temperature. This is another advantage of the current work compared to the antibody-based biosensors with limited storing capability at ambient temperature (Table S1). To guarantee the absence of carryover effects upon successive measurements on a single sensor, the repeatability of the biosensor was determined by DPV repetitive measurements (five times, n = 5) (Figure S6A), after 30 s incubation of 100 pg mL^{-1} H-FABP on the MIP electrode. Each experiment was repeated for three individual electrodes, and the relative standard deviation (RSD) was recorded as 2.71%, which is in an acceptable range. Another important feature for empirical applications of the biosensor is the reproducibility which was verified by recording the I_{pa} of $[Fe(CN)_6]^{3-/4-}$ for the five as-prepared MIP electrodes, each one three times with a total RSD of 5.57% (n = 5) (Figure S6B). A slight high value of this parameter can be related to the high surface roughness of the NMIs/ERGO electrode which can be effective on the distribution of the MIP layer and its thickness.

Interference Studies and the Performance of the MIP Biosensor in Serum and Plasma. Serum and cardiac biomarkers released during MI can interfere with H-FABP

https://dx.doi.org/10.1021/acssensors.0c01701
ACS Sens. 2021, 6, 797−807

Table 1. Summary of the Clinical Sample Investigation and Comparison of the Results of the Developed MIP Biosensor with the LFA Cassettes as a Reference Method

sample code	description of the clinical sample[a]	LFA (TnI)	LFA (H-FABP)	$(i_0 - i)/i_0$	H-FABP value[b]
sample 1	patient without MI symptoms	negative	negative	0.15 ± 0.02	≪ 10 pg mL^{-1}
sample 2	patient without MI symptoms	negative	negative	0.12 ± 0.05	≪ 10 pg mL^{-1}
sample 3	TnI ∼ 36.1	positive	negative	0.29 ± 0.04	<10 pg mL^{-1}
sample 4	negative troponin but MI occurred	negative	positive	0.68 ± 0.05	∼10 ng mL^{-1}
sample 5	negative troponin but MI occurred	negative	negative	0.50 ± 0.05	<10 pg mL^{-1}
sample 6	TnI > 50,000	positive	positive	0.36 ± 0.06	<10 pg mL^{-1}
sample 7	negative troponin but MI occurred	negative	positive	0.70 ± 0.05	∼30 ng mL^{-1}
sample 8	TnI ∼ 27.7	positive	negative	0.26 ± 0.05	<10 pg mL^{-1}

[a]Troponin levels were the approximate values determined by ELISA at the hospital. MI occurrence was detected by chest pain and ST-segment elevation. [b]The approximate values of H-FABP measured by the developed MIP biosensor. The values were determined through comparison of the recorded $(i_0 - i)/i_0$ for 10 times diluted clinical serum samples with the calibration plot of HS-10D spiked with various concentrations of H-FABP (Figure 4E).

during the detection.[66,67] As such, we investigated the performance of the developed biosensor in nonspiked HS (Figure S7A). To reduce the interference from high concentration of other proteins such as albumin, globulin, and fibrinogen inside the serum, we diluted the as-received HS with PBS.[68,69] There is no distinguishing difference between 10 and 100 times diluted HS. Therefore, 10 times diluted HS (HS-10D) was chosen for selectivity investigations. We also investigated the selectivity of the biosensor versus 100 pg mL^{-1} of each one of H-FABP (M_W = 15 kDa), myoglobin (Myo: M_W = 17.67 kDa), and troponin T (TnT: M_W = 35 kDa) in 10 mM PBS and HS-10D. Moreover, the interference effects of Myo and TnT during detection of H-FABP were examined using three different solutions containing 100 pg mL^{-1} H-FABP + 1 ng mL^{-1} TnT, 100 pg mL^{-1} H-FABP + 1 ng mL^{-1} Myo, and 100 pg mL^{-1} H-FABP + 1 ng mL^{-1} TnT + 1 ng mL^{-1} Myo in PBS and HS-10D (Figures 4D and S7B,C). In this regard, protein solutions were incubated on the MIP electrodes for 30 s. The electrodes were rinsed with DIW and then dried at ambient temperature. Eventually, I_{pa} of $[Fe(CN)_6]^{3-/4-}$ was recorded based on the DPV measurements. Overall, it is concluded that the interference of Myo (17.67 kDa), as another early biomarker of MI, with H-FABP (15 kDa) is slightly higher than TnT, mainly due to their approximately similar molecular weight and shape.[70] Figure S7D depicts the schematic illustration of simulated three-dimensional structures of cardiac and major serum proteins.[69]

To demonstrate the feasibility of the MIP biosensor for practical applications, we assessed the biosensor performance in HS, HP, and BS, where BS can also contain H-FABP.[71,72] The usual clinical range for H-FABP measurements is between pg mL^{-1} to several hundred ng mL^{-1}, and the general concentration of H-FABP in human serum is 3.9 ng mL^{-1} for normal adult individuals.[64] Thus, we spiked the as-received and 10 times diluted (10D) HS, HP, and BS with H-FABP in the range of 10 pg mL^{-1} to 100 ng mL^{-1}, which are shown in Figure 4E,F, and 4G, respectively. After incubating the spiked samples on the electrode surface for 30 s and rinsing with DIW, the I_{pa} of $[Fe(CN)_6]^{3-/4-}$ was recorded using DPV measurement. Accordingly, a similar condition in three media can be observed (corresponding DPV results are presented in Figure S8). As expected, the 10 times diluted serum (plasma) presents higher sensitivity to H-FABP in the clinical range concentrations. A similar trend has been reported in other literature studies,[2,24,73,74] suggesting the importance of serum (plasma) dilution to reduce the background noises. Interestingly, the current MIP assay demonstrates better performance in 10 times diluted serum (plasma) owing to the large active area, competed to the other MIP biosensors which merely work in more diluted serum and plasma (up to 100 times dilution).[2,24,73,74] Moreover, based on the previously reported H-FABP MIP biosensor,[16] we compared the results of the developed biosensor with a valid recorded enzyme-linked immunosorbent assay (ELISA) for H-FABP (as a reference method).[75] For this assay, the recovery values in 10 times diluted HP were recorded as 97−113%. Therefore, we calculated the recovery values of the MIP biosensor in HS, HP, and BS, each one 10 times diluted with 10 mM PBS and spiked with a range of H-FABP (10 pg mL^{-1} to 100 ng mL^{-1}). The results presented in Table S2 show that the recovery values in HP (91.7 ± 4.0−109.1 ± 7.5%) are approximately close to the reference method,[75] describing the potential of the biosensor for clinical applications.

Detection of H-FABP in Clinical Samples. Next, we explored the performance of the MIP biosensor for detection of H-FABP in clinical samples. Eight clinical blood serums samples were tested using commercial LFA cassettes and the MIP biosensor (Figure 4H,I, and Table 1). The positive control (Pos. Ctrl) sample was HS-10D spiked with 100 ng mL^{-1} H-FABP. The clinical samples without MI symptoms showed very low $(i_0 - i)/i_0$ and tested negative H-FABP and TnI on LFA cassettes (samples 1 and 2) which made them as the negative control (Neg. Ctrl). The two samples (samples 3 and 8) tested negative H-FABP and positive TnI on LFA cassettes and demonstrated low $(i_0 - i)/i_0$ (less than 0.4) compared with the Pos. Ctrl, while showed higher $(i_0 - i)/i_0$ in comparison with the Neg. Ctrl. This implies that the level of H-FABP is lower than 8 ng mL^{-1} (the LOD of the LFA for H-FABP, provided by the company) in these serums. Furthermore, comparing these results with standard calibration plots of H-FABP in HS-10D (Figure 4E) revealed that the levels of H-FABP in these samples are lower than 10 pg mL^{-1}, despite the negligible interference from TnI. Sample 5 (tested negative for H-FABP and TnI) showed higher $(i_0 - i)/i_0$ (approximately 0.5). According to the calibration plot (Figure 4E), the level of H-FABP in this sample is lower than 10 pg mL^{-1}; thus, the LFA cassette cannot detect it. This clearly highlights the benefits of the developed biosensor with a lower LOD than the commercial device.

The other two samples (samples 4 and 7) that tested positive H-FABP on the LFA cassettes displayed $(i_0 - i)/i_0$ close to the Pos. Ctrl, confirming the ability of the device to

https://dx.doi.org/10.1021/acssensors.0c01701
ACS Sens. 2021, 6, 797−807

reliably detect H-FABP in clinical samples with levels higher than 1 ng mL^{-1}. Sample 6 tested positive for H-FABP and TnI by LFA. However, the $(i_0 - i)/i_0$ recorded by the biosensor was less than 0.4, mainly related to the rather weak performance of the biosensor in high concentrated serum (the TnI value for this sample was recorded to be more than 50,000 ng mL^{-1} according to Table 1). Consequently, while the LFA needs expensive bioreceptors (antibodies) and has a longer analysis time (~10 min) and a high detection limit, the cost-effective MIP biosensor can successfully and specifically detect significantly lower levels of H-FABP in clinical samples, in less than 1 min.

Overall, the results of this study indicate that the developed MIP biosensor offers acceptable sensitivity, stability, repeatability, and reproducibility toward protein detection. We confirm that the integration of NMIs with MIP improves the limitations of MIP-based biosensors such as low sensitivity and the difficulties in the fabrication process. The selectivity of the proposed biosensor in undiluted serum (plasma), however, needs further improvement. Therefore, we intend to investigate the performance of other nonconductive monomers for electropolymerization such as *p*-aminothiophenol or dopamine and use aptamer/MIP combinations for improving the selectivity.

CONCLUSIONS

In summary, we developed an electrochemical biosensor based on a core−shell structure of NMIs and MIP for detection of H-FABP in PBS, human plasma, human serum, and bovine serum via a hybrid electrodeposition/electropolymerization fabrication protocol. We found that the size and morphology of NMIs are tunable via electrodeposition. The results suggested that the ERGO improved nucleation of NMIs and provided uniform distribution of gold on the surface due to the increase in the electrode surface area. The electropolymerization of o-PD on NMIs was successfully optimized to reach the core−shell structure. Our study indicated that gold NMIs facilitated the template H-FABP removal process from the polymeric matrix during washing with ethanol and water at ambient temperature by reducing the template removal time to less than 1 min.

The proposed biosensor was used to detect H-FABP as one of the early biomarkers of myocardial infarction with concentrations lower than 10 fg mL^{-1} in PBS and in a short period of time (30 s). Due to the large active area of NMIs/ERGO, this biosensor showed a lower LOD and wider linear range of detection than the commercial H-FABP LFA cassette. The selectivity evaluations also indicated distinguishable detection of H-FABP among other cardiac biomarkers and in clinical samples owing to the biomimetic MIP layer. Moreover, the polymeric nature of the MIP layer provided high stability of the proposed biosensor at ambient temperature up to 3 weeks, depicting its excellent storage ability than the previously reported antibody-based biosensors that are usually stored at 4 °C.[45,76,77] However, the performance of the biosensor in undiluted serum samples and the electrochemical setup for point-of-care applications need to be improved in future investigations. As MIP biosensors are more stable, more efficient, and more scalable, than antibody-based biosensors at ambient temperature and in clinical environments, this biosensor combination can be considered for fast, sensitive, and affordable detection of proteins in future studies.

ASSOCIATED CONTENT

Supporting Information

The Supporting Information is available free of charge at https://pubs.acs.org/doi/10.1021/acssensors.0c01701.

Details of the electrode fabrication methods including electrochemical reduction of graphene oxide, electropolymerization of o-PD, H-FABP template removal process, and recovery calculations (PDF)

AUTHOR INFORMATION

Corresponding Author

Sara Mahshid − *Department of Bioengineering, McGill University, Montreal, Quebec H3A 0E9, Canada;* orcid.org/0000-0003-4203-819X; Email: sara.mahshid@mcgill.ca

Authors

Alireza Sanati − *Department of Bioengineering, McGill University, Montreal, Quebec H3A 0E9, Canada; Department of Materials Engineering, Isfahan University of Technology, Isfahan 84156-83111, Iran; Department of Anatomy and Cell Biology, McGill University, Montreal, Quebec H3A 0C7, Canada; Biosensor Research Center, School of Advanced Technologies in Medicine, Isfahan University of Medical Sciences, Isfahan 81746-73461, Iran;* orcid.org/0000-0001-5722-9541

Roozbeh Siavash Moakhar − *Department of Bioengineering, McGill University, Montreal, Quebec H3A 0E9, Canada;* orcid.org/0000-0001-8334-085X

Imman I. Hosseini − *Department of Bioengineering, McGill University, Montreal, Quebec H3A 0E9, Canada*

Keyvan Raeissi − *Department of Materials Engineering, Isfahan University of Technology, Isfahan 84156-83111, Iran*

Fathallah Karimzadeh − *Department of Materials Engineering, Isfahan University of Technology, Isfahan 84156-83111, Iran*

Mahsa Jalali − *Department of Bioengineering, McGill University, Montreal, Quebec H3A 0E9, Canada;* orcid.org/0000-0003-2353-3910

Mahshid Kharaziha − *Department of Materials Engineering, Isfahan University of Technology, Isfahan 84156-83111, Iran;* orcid.org/0000-0002-8803-105X

Sara Sheibani − *Department of Anatomy and Cell Biology, McGill University, Montreal, Quebec H3A 0C7, Canada*

Laleh Shariati − *Department of Biomaterials, Nanotechnology, and Tissue Engineering, School of Advanced Technologies in Medicine and Applied Physiology Research Center, Isfahan University of Medical Sciences, Isfahan 81746-73461, Iran*

John F. Presley − *Department of Anatomy and Cell Biology, McGill University, Montreal, Quebec H3A 0C7, Canada*

Hojatollah Vali − *Department of Anatomy and Cell Biology, McGill University, Montreal, Quebec H3A 0C7, Canada*

Complete contact information is available at: https://pubs.acs.org/10.1021/acssensors.0c01701

Notes

The authors declare no competing financial interest.

ACKNOWLEDGMENTS

The authors thank the Faculty of Engineering at McGill University, the Natural Science and Engineering Research Council of Canada (NSERC, G247765), the Canada

Foundation for Innovation (CFI, G248924) and MI4 (McGill Interdisciplinary Initiative in Infection and Immunity) for financial support. The authors acknowledge Nanotools Microfab and the Facility for Electron Microscopy Research at McGill University and the research facilities of NanoQAM at the Université du Québec à Montréal. Also, we sincerely thank Dr. Elham Bidram from the School of Advanced Technologies in Medicine, Isfahan University of Medical Sciences, for providing the ethical authority for working with clinical samples.

REFERENCES

(1) Gui, R.; Jin, H.; Guo, H.; Wang, Z. Recent advances and future prospects in molecularly imprinted polymers-based electrochemical biosensors. *Biosens. Bioelectron.* **2018**, *100*, 56−70.
(2) Tancharoen, C.; Sukjee, W.; Thepparit, C.; Jaimipuk, T.; Auewarakul, P.; Thitithanyanont, A.; Sangma, C. Electrochemical Biosensor Based on Surface Imprinting for Zika Virus Detection in Serum. *ACS Sens.* **2019**, *4*, 69−75.
(3) Lofgreen, J. E.; Moudrakovski, I. L.; Ozin, G. A. Molecularly Imprinted Mesoporous Organosilica. *ACS Nano* **2011**, *5*, 2277−2287.
(4) Ren, K.; Zare, R. N. Chemical Recognition in Cell-Imprinted Polymers. *ACS Nano* **2012**, *6*, 4314−4318.
(5) Kalecki, J.; Cieplak, M.; Dąbrowski, M.; Lisowski, W.; Kuhn, A.; Sharma, P. S. Hexagonally Packed Macroporous Molecularly Imprinted Polymers for Chemosensing of Follicle-Stimulating Hormone Protein. *ACS Sens.* **2020**, *5*, 118−126.
(6) Bergmann, N. M.; Peppas, N. A. Molecularly imprinted polymers with specific recognition for macromolecules and proteins. *Prog. Polym. Sci.* **2008**, *33*, 271−288.
(7) Uzun, L.; Turner, A. P. F. Molecularly-imprinted polymer sensors: realising their potential. *Biosens. Bioelectron.* **2016**, *76*, 131−144.
(8) Zeng, Z.; Hoshino, Y.; Rodriguez, A.; Yoo, H.; Shea, K. J. Synthetic Polymer Nanoparticles with Antibody-like Affinity for a Hydrophilic Peptide. *ACS Nano* **2010**, *4*, 199−204.
(9) Haupt, K.; Mosbach, K. Molecularly imprinted polymers and their use in biomimetic sensors. *Chem. Rev.* **2000**, *100*, 2495−2504.
(10) Ma, Y.; Li, W.; Xing, R.; Li, P.; Liu, Z. Epitope-Imprinted Magnetic Nanoparticles as a General Platform for Efficient in Vitro Evolution of Protein-Binding Aptamers. *ACS Sens.* **2020**, *5*, 2537−2544.
(11) Zhang, Z.; Liu, J. Molecular Imprinting with Functional DNA. *Small* **2019**, *15*, 1805246.
(12) Ghanbari, K.; Roushani, M. A nanohybrid probe based on double recognition of an aptamer MIP grafted onto a MWCNTs-Chit nanocomposite for sensing hepatitis C virus core antigen. *Sens. Actuators, B* **2018**, *258*, 1066−1071.
(13) Lu, X.; Zhou, G.; Zhang, J.; Xie, W.; Yang, Y.; Zeng, Y.; Zhang, Z.; Wang, H.; Li, L. Highly Sensitive Determination of 2,4,6-Trichlorophenol by Using a Novel SiO_2@MIPIL Fluorescence Sensor with a Double Recognition Functional Monomer. *ACS Sens.* **2020**, *5*, 1445−1454.
(14) Mahmoudpour, M.; Torbati, M.; Mousavi, M.-M.; de la Guardia, M.; Ezzati Nazhad Dolatabadi, J. Nanomaterial-based molecularly imprinted polymers for pesticides detection: Recent trends and future prospects. *TrAC, Trends Anal. Chem.* **2020**, *129*, 115943.
(15) Ma, Y.; Shen, X.-L.; Zeng, Q.; Wang, L.-S. A glassy carbon electrode modified with graphene nanoplatelets, gold nanoparticles and chitosan, and coated with a molecularly imprinted polymer for highly sensitive determination of prostate specific antigen. *Microchim. Acta* **2017**, *184*, 4469−4476.
(16) Crapnell, R. D.; Czulak, J.; Johnson, R.; Betlem, K.; Mecozzi, F.; Down, M. P.; Eersels, K.; van Grinsven, B.; Cleij, T. J.; Law, R.; Banks, C. E.; Peeters, M.; Peeters, M. Thermal Detection of Cardiac Biomarkers Heart-Fatty Acid Binding Protein and ST2 Using a Molecularly Imprinted Nanoparticle-Based Multiplex Sensor Platform. *ACS Sens.* **2019**, *4*, 2838−2845.
(17) Liu, X.; Lin, W.; Xiao, P.; Yang, M.; Sun, L.-P.; Zhang, Y.; Xue, W.; Guan, B.-O. Polydopamine-based molecular imprinted optic microfiber sensor enhanced by template-mediated molecular rearrangement for ultra-sensitive C-reactive protein detection. *Chem. Eng. J.* **2020**, *387*, 124074.
(18) Johari-Ahar, M.; Karami, P.; Ghanei, M.; Afkhami, A.; Bagheri, H. Development of a molecularly imprinted polymer tailored on disposable screen-printed electrodes for dual detection of EGFR and VEGF using nanoliposomal amplification strategy. *Biosens. Bioelectron.* **2018**, *107*, 26−33.
(19) Kidakova, A.; Boroznjak, R.; Reut, J.; Öpik, A.; Saarma, M.; Syritski, V. Molecularly imprinted polymer-based SAW sensor for label-free detection of cerebral dopamine neurotrophic factor protein. *Sens. Actuators, B* **2020**, *308*, 127708.
(20) Kidakova, A.; Reut, J.; Boroznjak, R.; Öpik, A.; Syritski, V. Advanced sensing materials based on molecularly imprinted polymers towards developing point-of-care diagnostics devices. *Proc. Est. Acad. Sci.* **2019**, *68*, 158−167.
(21) Boroznjak, R.; Reut, J.; Tretjakov, A.; Lomaka, A.; Öpik, A.; Syritski, V. A computational approach to study functional monomer-protein molecular interactions to optimize protein molecular imprinting. *J. Mol. Recognit.* **2017**, *30*, No. e2635.
(22) Kidakova, A.; Reut, J.; Rappich, J.; Öpik, A.; Syritski, V. Preparation of a surface-grafted protein-selective polymer film by combined use of controlled/living radical photopolymerization and microcontact imprinting. *React. Funct. Polym.* **2018**, *125*, 47−56.
(23) Karami, P.; Bagheri, H.; Johari-Ahar, M.; Khoshsafar, H.; Arduini, F.; Afkhami, A. Dual-modality impedimetric immunosensor for early detection of prostatespecific antigen and myoglobin markers based on antibody-molecularly imprinted polymer. *Talanta* **2019**, *202*, 111−122.
(24) Pacheco, J. G.; Rebelo, P.; Freitas, M.; Nouws, H. P. A.; Delerue-Matos, C. Breast cancer biomarker (HER2-ECD) detection using a molecularly imprinted electrochemical sensor. *Sens. Actuators, B* **2018**, *273*, 1008−1014.
(25) Yola, M. L.; Atar, N. Development of cardiac troponin-I biosensor based on boron nitride quantum dots including molecularly imprinted polymer. *Biosens. Bioelectron.* **2019**, *126*, 418−424.
(26) Couto, R. A. S.; Costa, S. S.; Mounssef, B., Jr.; Pacheco, J. G.; Fernandes, E.; Carvalho, F.; Rodrigues, C. M. P.; Delerue-Matos, C.; Braga, A. A. C.; Moreira Gonçalves, L.; Quinaz, M. B. Electrochemical sensing of ecstasy with electropolymerized molecularly imprinted poly(o-phenylenediamine) polymer on the surface of disposable screen-printed carbon electrodes. *Sens. Actuators, B* **2019**, *290*, 378−386.
(27) Golabi, M.; Kuralay, F.; Jager, E. W. H.; Beni, V.; Turner, A. P. F. Electrochemical bacterial detection using poly(3-aminophenylboronic acid)-based imprinted polymer. *Biosens. Bioelectron.* **2017**, *93*, 87−93.
(28) Lu, H.; Xu, S.; Liu, J. One Pot Generation of Blue and Red Carbon Dots in One Binary Solvent System for Dual Channel Detection of Cr^{3+} and Pb^{2+} Based on Ion Imprinted Fluorescence Polymers. *ACS Sens.* **2019**, *4*, 1917−1924.
(29) Karimian, N.; Stortini, A. M.; Moretto, L. M.; Costantino, C.; Bogialli, S.; Ugo, P. Electrochemosensor for Trace Analysis of Perfluorooctanesulfonate in Water Based on a Molecularly Imprinted Poly(o-phenylenediamine) Polymer. *ACS Sens.* **2018**, *3*, 1291−1298.
(30) Beluomini, M. A.; Karimian, N.; Stradiotto, N. R.; Ugo, P. Tailor-made 3D-nanoelectrode ensembles modified with molecularly imprinted poly(o-phenylenediamine) for the sensitive detection of L-arabitol. *Sens. Actuators, B* **2019**, *284*, 250−257.
(31) Kor, K.; Zarei, K. Development and characterization of an electrochemical sensor for furosemide detection based on electropolymerized molecularly imprinted polymer. *Talanta* **2016**, *146*, 181−187.

https://dx.doi.org/10.1021/acssensors.0c01701
ACS Sens. 2021, 6, 797−807

(32) Wackerlig, J.; Schirhagl, R. Applications of MIP nanoparticles and their advances towards industrial use − A Review. *Anal. Chem.* **2016**, *88*, 250−261.
(33) Lv, Y.; Tan, T.; Svec, F. Molecular imprinting of proteins in polymers attached to the surface of nanomaterials for selective recognition of biomacromolecules. *Biotechnol. Adv.* **2013**, *31*, 1172−1186.
(34) Ahmad, R.; Griffete, N.; Lamouri, A.; Felidj, N.; Chehimi, M. M.; Mangeney, C. Nanocomposites of gold nanoparticles@molecularly imprinted polymers: Chemistry, processing, and applications in sensors. *Chem. Mater.* **2015**, *27*, 5464−5478.
(35) Matsui, J.; Akamatsu, K.; Nishiguchi, S.; Miyoshi, D.; Nawafune, H.; Tamaki, K.; Sugimoto, N. Composite of Au Nanoparticles and Molecularly Imprinted Polymer as a Sensing Material. *Anal. Chem.* **2004**, *76*, 1310−1315.
(36) Jalali, M.; AbdelFatah, T.; Mahshid, S. S.; Labib, M.; Sudalaiyadum Perumal, A.; Mahshid, S. A hierarchical 3D nanostructured microfluidic device for sensitive detection of pathogenic bacteria. *Small* **2018**, *14*, 1801893.
(37) Mahshid, S. S.; Mahshid, S.; Vallée-Bélisle, A.; Kelley, S. O. Peptide-mediated electrochemical steric hindrance assay for one-step detection of HIV antibodies. *Anal. Chem.* **2019**, *91*, 4943−4947.
(38) Siavash Moakhar, R.; AbdelFatah, T.; Sanati, A.; Jalali, M.; Flynn, S. E.; Mahshid, S. S.; Mahshid, S. A Nanostructured Gold/Graphene Microfluidic Device for Direct and Plasmonic-Assisted Impedimetric Detection of Bacteria. *ACS Appl. Mater. Interfaces* **2020**, *12*, 23298−23310.
(39) Mahshid, S.; Mepham, A. H.; Mahshid, S. S.; Burgess, I. B.; Saberi Safaei, T.; Sargent, E. H.; Kelley, S. O. Mechanistic control of the growth of three-dimensional gold sensors. *J. Phys. Chem. C* **2016**, *120*, 21123−21132.
(40) Jalali, M.; Filine, E.; Dalfen, S.; Mahshid, S. Microscale reactor embedded with Graphene/hierarchical gold nanostructures for electrochemical sensing: application to the determination of dopamine. *Microchim. Acta* **2020**, *187*, 90.
(41) Jalali, M.; Moakhar, R. S.; Abdelfattah, T.; Filine, E.; Mahshid, S. S.; Mahshid, S. Nanopattern-Assisted Direct Growth of Peony-like 3D MoS_2/Au Composite for Nonenzymatic Photoelectrochemical Sensing. *ACS Appl. Mater. Interfaces* **2020**, *12*, 7411−7422.
(42) Mahshid, S. S.; Flynn, S. E.; Mahshid, S. The potential application of electrochemical biosensors in the COVID-19 pandemic: A perspective on the rapid diagnostics of SARS-CoV-2. *Biosens. Bioelectron.* **2021**, *176*, 112905−112914.
(43) Maurice, M. A. L.; Hermens, W. T.; Glatz, J. F. C. Fatty acid-binding proteins as plasma markers of tissue injury. *Clin. Chim. Acta* **2005**, *352*, 15−35.
(44) Delle, L. E.; Pachauri, V.; Sharma, S.; Shaforost, O.; Ma, H.; Adabi, M.; Lilischkis, R.; Wagner, P.; Thoelen, R.; Klein, N.; O'Kennedy, R.; Ingebrandt, S. ScFv-modified graphene-coated IDE-arrays for "label-free" screening of cardiovascular disease biomarkers in physiological saline. *Biosens. Bioelectron.* **2018**, *102*, 574−581.
(45) Mihailescu, C.-M.; Stan, D.; Iosub, R.; Moldovan, C.; Savin, M. A Sensitive capacitive immunosensor for direct detection of human heart fatty acid-binding protein (h-FABP). *Talanta* **2015**, *132*, 37−43.
(46) Stan, D.; Mihailescu, C.-M.; Iosub, R.; Moldovan, C.; Savin, M.; Baciu, I. Electrochemical studies of homogeneous self-assembled monolayers versus mixed self-assembled monolayers on gold electrode for "label free" detection of heart fatty acid binding protein. *Thin Solid Films* **2012**, *526*, 143−149.
(47) Forootan Rostamabadi, P.; Heydari-Bafrooei, E. Impedimetric aptasensing of the breast cancer biomarker HER2 usin a glassy carbon electrode modified with gold nanoparticles in a composite consisting of electrochemically reduced graphene oxide and single-walled carbon nanotubes. *Microchim. Acta* **2019**, *186*, 495.
(48) Berbeć, S.; Żołądek, S.; Jabłońska, A.; Pałys, B. Electrochemically reduced graphene oxide on gold nanoparticles modified with a polyoxomolybdate film. Highly sensitivenon-enzymatic electrochemical detection of H_2O_2. *Sens. Actuators, B* **2018**, *258*, 745−756.
(49) Sanati, A.; Raeissi, K.; Karimzadeh, F. A cost-effective and green-reduced graphene oxide/polyurethane foam electrode for electrochemical applications. *FlatChem* **2020**, *20*, 100162.
(50) Desireddy, A.; Conn, B. E.; Guo, J.; Yoon, B.; Barnett, R. N.; Monahan, B. M.; Kirschbaum, K.; Griffith, W. P.; Whetten, R. L.; Landman, U.; Bigioni, T. P. Ultrastable silver nanoparticles. *Nature* **2013**, *501*, 399−402.
(51) Kumar, S. A.; Chen, S. M. Nanostructured Zinc Oxide Particles in Chemically Modified Electrodes for Biosensor Applications. *Anal. Lett.* **2008**, *41*, 141−158.
(52) Sarkar, A.; Ghosh, A. B.; Saha, N.; Bhadu, G. R.; Adhikary, B. Newly Designed Amperometric Biosensor for Hydrogen Peroxide and Glucose Based on Vanadium Sulfide Nanoparticles. *ACS Appl. Nano Mater.* **2018**, *1*, 1339−1347.
(53) Liu, B.; Liu, J. Sensors and biosensors based on metal oxide nanomaterials. *TrAC, Trends Anal. Chem.* **2019**, *121*, 115690.
(54) Campuzano, S.; Yáñez-Sedeño, P.; Pingarrón, J. M. Carbon Dots and Graphene Quantum Dots in Electrochemical Biosensing. *Nanomaterials* **2019**, *9*, 634.
(55) Gomes, R. S.; Moreira, F. T. C.; Fernandes, R.; Sales, M. G. F. Sensing CA 15-3 in point-of-care by electropolymerizing O-phenylenediamine (oPDA) on Au-screen printed electrodes. *PLoS One* **2018**, *13*, No. e0196656.
(56) Karimian, N.; Turner, A. P. F.; Tiwari, A. Electrochemical evaluation of troponin T imprinted polymer receptor. *Biosens. Bioelectron.* **2014**, *59*, 160−165.
(57) Valera, A. E.; Nesbitt, N. T.; Archibald, M. M.; Naughton, M. J.; Chiles, T. C. On-Chip Electrochemical Detection of Cholera Using a Polypyrrole-Functionalized Dendritic Gold Sensor. *ACS Sens.* **2019**, *4*, 654−659.
(58) Du, X.; Zhang, Z.; Miao, Z.; Ma, M.; Zhang, Y.; Zhang, C.; Wang, W.; Han, B.; Chen, Q. One step electrodeposition of dendritic gold nanostructures on β-lactoglobulin-functionalized reduced graphene oxide for glucose sensing. *Talanta* **2015**, *144*, 823−829.
(59) Liu, M.; Pang, Y.; Zhang, B.; De Luna, P.; Voznyy, O.; Xu, J.; Zheng, X.; Dinh, C. T.; Fan, F.; Cao, C.; de Arquer, F. P. G.; Safaei, T. S.; Mepham, A.; Klinkova, A.; Kumacheva, E.; Filleter, T.; Sinton, D.; Kelley, S. O.; Sargent, E. H. Enhanced electrocatalytic CO_2 reduction via field-induced reagent concentration. *Nature* **2016**, *537*, 382−386.
(60) Mariano, R. G.; McKelvey, K.; White, H. S.; Kanan, M. W. Selective increase in CO_2 electroreduction activity at grain-boundary surface terminations. *Sciecne* **2017**, *358*, 1187−1192.
(61) Sun, J.; Wang, F.; Liu, Y.; Ni, Y.; Zhou, H.; Guo, C. F.; Chen, S. Gold micromeshes as highly active electrocatalysts for methanol oxidation reaction. *RSC Adv.* **2017**, *7*, 22479−22484.
(62) Amatatongchai, M.; Sroysee, W.; Jarujamrus, P.; Nacapricha, D.; Lieberzeit, P. A.; Lieberzeit, P. A. Selective amperometric flow-injection analysis of carbofuran using a molecularly-imprinted polymer and gold-coated-magnetite modified carbon nanotube-paste electrode. *Talanta* **2018**, *179*, 700−709.
(63) Guider, R.; Gandolfi, D.; Chalyan, T.; Pasquardini, L.; Samusenko, A.; Pederzolli, C.; Pucker, G.; Pavesi, L. Sensitivity and limit of detection of biosensors based on ring resonators. *Sens. Biosens. Res.* **2015**, *6*, 99−102.
(64) McCann, C. J.; Glover, B. M.; Menown, I. B. A.; Moore, M. J.; McEneny, J.; Owens, C. G.; Smith, B.; Sharpe, P. C.; Young, I. S.; Adgey, J. A. Novel biomarkers in early diagnosis of acute myocardial infarction compared with cardiac troponin T. *Eur. Heart J.* **2008**, *29*, 2843−2850.
(65) Bhalla, N.; Pan, Y.; Yang, Z.; Payam, A. F. Opportunities and Challenges for Biosensors and Nanoscale Analytical Tools for Pandemics: COVID-19. *ACS Nano* **2020**, *14*, 7783−7807.
(66) Ladenson, J. H. A personal history of markers of myocyte injury myocardial infarction. *Clin. Chim. Acta* **2007**, *381*, 3−8.
(67) David, J. K.; Diana, L. Serum markers in the emergency department diagnosis of acute myocardial infarction. *Emerg. Med. Clin.* **2001**, *19*, 321−337.
(68) Flodin, P.; Killander, J. Fractionation Of Human-Serum Proteins By Gel Filtration. *Biochim. Biophys. Acta* **1962**, *63*, 403−410.

https://dx.doi.org/10.1021/acssensors.0c01701
ACS Sens. 2021, 6, 797−807

(69) Smith, G. S.; Walter, G. L.; Walker, R. M. Clinical Pathology in Non-Clinical Toxicology Testing. *Haschek and Rousseaux's Handbook of Toxicologic Pathology*; Academic Press: Boston, 2013; Chapter 18, pp 565−594.
(70) Adeel, M.; Rahman, M. M.; Lee, J.-J. Label-free aptasensor for the detection of cardiac biomarker myoglobin based on gold nanoparticles decorated boron nitride nanosheets. *Biosens. Bioelectron.* **2019**, *126*, 143−150.
(71) Billich, S.; Wissel, T.; Kratzin, H.; Hahn, U.; Hagenhoff, B.; Lezius, A. G.; Spener, F. Cloning of a full-length complementary DNA for fatty-acid-binding protein from bovine heart. *Eur. J. Biochem.* **1988**, *175*, 549−556.
(72) Lassen, D.; Lücke, C.; Kromminga, A.; Lezius, A.; Spener, F.; Rüterjans, H. Solution structure of bovine heart fatty acid-binding protein (H-FABP). *Mol. Cell. Biochem.* **1993**, *123*, 15−22.
(73) Shumyantseva, V. V.; Bulko, T. V.; Sigolaeva, L. V.; Kuzikov, A. V.; Archakov, A. I. Electrosynthesis and binding properties of molecularly imprinted poly-o-phenylene diamine for selective recognition and direct electrochemical detection of myoglobin. *Biosens. Bioelectron.* **2016**, *86*, 330−336.
(74) Karimian, N.; Vagin, M.; Zavar, M. H. A.; Chamsaz, M.; Turner, A. P. F.; Tiwari, A. An ultrasensitive molecularly-imprinted human cardiac troponin sensor. *Biosens. Bioelectron.* **2013**, *50*, 492−498.
(75) Wodzig, K. W. H.; Pelsers, M. M. A. L.; Van Der Vusse, G. J.; Roos, W.; Glatz, J. F. C. One-Step Enzyme-Linked Immunosorbent Assay (ELISA) for Plasma Fatty Acid-Binding Protein. *Ann. Clin. Biochem.* **1997**, *34*, 263.
(76) Qin, X.; Xu, A.; Liu, L.; Sui, Y.; Li, Y.; Tan, Y.; Chen, C.; Xie, Q. Selective staining of CdS on ZnO biolabel for ultrasensitive sandwich-type amperometric immunoassay of human heart-type fatty-acid-binding protein and immunoglobulin G. *Biosens. Bioelectron.* **2017**, *91*, 321−327.
(77) Agarwal, D. K.; Prasad, A.; Vinchurkar, M.; Gandhi, S.; Prabhakar, D.; Mukherji, S.; Rao, V. R. Detection of heart-type fatty acid-binding protein (h-FABP) using piezoresistive polymer micro-cantilevers functionalized by a dry method. *Appl. Nanosci.* **2018**, *8*, 1031−1042.

https://dx.doi.org/10.1021/acssensors.0c01701
ACS Sens. 2021, 6, 797−807